JMEPEG (2017) 26:2057–2071
DOI: 10.1007/s11665-017-2638-2

1059-9495/$19.00

Effect of Nickel Contents on the Microstructure and Mechanical Properties for Low-Carbon Bainitic Weld Metals

Gaojun Mao, Rui Cao, Jun Yang, Yong Jiang, Shuai Wang, Xili Guo, Junjun Yuan, Xiaobo Zhang, and Jianhong Chen

(Submitted October 9, 2016; in revised form December 14, 2016; published online April 3, 2017)

Multi-pass weld metals were deposited on Q345 base steel using metal powder-flux-cored wire with various Ni contents to investigate the effects of the Ni content on the weld microstructure and property. The types of the microstructures were identified by optical microscope, scanning electron microscope, transmission electron microscope, and micro-hardness tests. As a focusing point, the lath bainite and lath martensite were distinguished by their compositions, morphologies, and hardness. In particular, a number of black plane facets appearing between lath bainite or lath martensite packets were characterized by laser scanning confocal microscope. The results indicated that with the increase in Ni contents in the range of 0, 2, 4, and 6%, the microstructures in the weld-deposited metal were changed from the domination of the granular bainite to the majority of the lath bainite and/or the lath martensite and the micro-hardness of the weld-deposited metal increased. Meanwhile, the average width of columnar grain displays a decreasing trend and prior austenite grain size decreases while increases with higher Ni content above 4%. Yield strength and ultimate tensile strength decrease, while the reduction in fracture area increases with the decreasing Ni mass fraction and the increasing test temperature, respectively. And poor yield strength in Ni6 specimen can be attributed to elements segregation caused by weld defect. Finally, micro-hardness distribution in correspondence with specimens presents as a style of cloud-map.

Keywords black plane facets, micro-hardness, microstructure, multi-pass weld metals, Ni content, tensile property

1. Introduction

Nowadays, advanced steels developed by optimizing the alloy compositions and microstructure from ferrite plus pearlite through tempered martensite to extra-low-carbon lath bainite plus lath martensite can successfully achieve high strength of 1000 MPa and Charpy V toughness of 200 J at −40 °C (Ref 1). In addition, strictly thermo-mechanical controlling process, transformation-induced plasticity process, and reasonable heat treatment process for element partitioning further improve the performances (Ref 2). These steels with high strength and high toughness have been widely applied in the field of pipeline, ship building, and various manufacturing industries. However, due to the complexity of welding processes and limitations of thermal process of welding, the toughness of the weld metal in low temperature is much lower than that of the base metal. For X70, X80 pipeline steel, the impact toughness of the matched weld metal only reaches half or even lower by comparison with the Charpy V toughness of base metal (Ref 2). Worse still, the impact toughness of weld metal which were matched to E610E steel only reached one-third of that of the base material (Ref 2). There have been ongoing developments in high-strength steel weld metals with the aim of increasing strength while maintaining acceptable toughness since 1960s (Ref 3). The mechanical properties of weld metals are strongly dependent on the microstructure developed during solidification and cooling of the weld pool, which is determined by the weld chemical composition and cooling rate (Ref 4). The optimized microstructure of the weld metal for the X120 application consists of low-carbon lath martensite and lath bainite and/or their derivatives. Although too weak on its own, a minor presence of acicular ferrite (AF) was planned to improve the toughness (Ref 5).

For investigating the factors affecting the microstructure, it is of great significance to characterize the microstructures. In general, the microstructure of the low-carbon-deposited weld metal can consist of pro-eutectoid ferrite (PF), side-plated ferrite (SPF), acicular ferrite (AF), granular bainite (GB), lath bainite (LB), lath martensite (LM), and retained austenite (RA). The first four types of the microstructure are easier to be identified, and the RA was detected by TEM and quantified by X-ray analyses. It is rather difficult to distinguish LB and LM which were in several cases distinguished by using commercial software; however, the results seem to be not accurate. The characterization of lath bainite and lath martensite have been done by conventional metallographic methods such as compositions comparison (Ref 6), different microstructural morphology displayed by scanning electron microscope (SEM) (Ref 7) and transmission electron microscope (TEM) (Ref 8), micro-hardness (Ref 4), and electron back scattered diffraction (EBSD) (Ref 9).

Gaojun Mao, Rui Cao, Junjun Yuan, Xiaobo Zhang, and **Jianhong Chen**, State Key Laboratory of Advanced Processing and Recycling of Non-ferrous Metal, Lanzhou University of Technology, Lanzhou 730050, People's Republic of China; **Jun Yang** and **Shuai Wang**, State Key Laboratory of Solid Lubrication, Lanzhou Institute of Chemical Physics, Chinese Academy of Sciences, Lanzhou 730000, People's Republic of China; and **Yong Jiang** and **Xili Guo**, Atlantic China Welding Concumables, Inc, Zigong 643000, People's Republic of China. Contact e-mails: caorui@lut.cn and zchen@lut.cn.

In addition, in the microstructure of low-carbon high-strength weld metal, a number of black facets appear between the packets of lath bainite or lath martensite as shown by the white arrows in Fig. 1. These black facets were claimed as coalesced bainite (Ref 10) and tempered martensite (Ref 11). Because these black facets occupy a large part of area, it is necessary to identify their characters.

Among the alloying elements of low-carbon martensite/bainite steels, an increase in Ni content was found to be the effective way to improve both the strength and the fracture toughness (Ref 12). Small columnar grains were associated with a Ni_{eq} between 3.4 and 6.2% which would result in a peritectic reaction when the weld melt solidified, while a Ni_{eq} higher than 6.2% would generate very large columnar grains as the liquid in the weld pool would directly solidify into austenite and have a continuous growth afterward (Ref 13). In addition, the existence of Ni can raise T_0 (Ref 14), one temperature when there exists identical carbon content for both ferrite and austenite under the condition of quasi-equilibrium, which is conducive to the formation of the sheet retained austenite and carbonless lath bainite and reduction of large matensite–austenite (M-A) blocks (Ref 15). In the multi-pass welded joints, the main reason that makes weld toughness appear volatility was attributed to the coarse columnar grains in the as-deposited weld metal and to the coarse grains in the heat-affected zone (HAZ) (Ref 16), while adding Ni can effectively reduce this volatility. It has been widely recognized that Ni can improve the toughness of the welded joint of high-strength steel; however, its mechanism has not been studied clearly, and especially the role that Ni playing on bainite formation needs further study. Therefore, it will come to outstanding scientific values and prospects to make sense how the different contents of Ni in weld metal affect the microstructure and properties of the weld. Some authors have reported an effect of the presence of coarse grains on the ultimate tensile strength (UTS), but their effect on the yield stress is reported to be more limited (Ref 14).

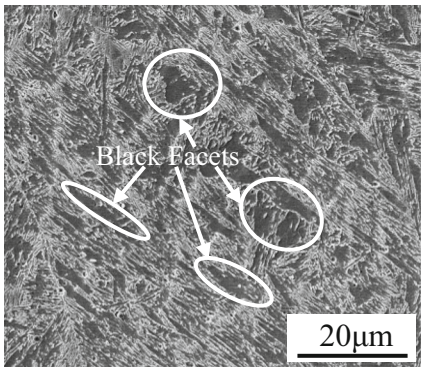

Fig. 1 Microstructure showing the lath martensite with black plane facets between the packets by SEM

In this paper, at first the phase components which could appear in the low-carbon high-strength weld metal are characterized by incorporating following methods: chemical composition analyses, comparison of microstructural morphology displayed by SEM and TEM, micro-hardness tests and analyses of the relief revealed by the laser scanning confocal microscope (LSCM). By means of these ways, the macro- and microstructure of real weld metal deposited by metal powder-flux-cored wires with various Ni contents ranged from 0 to 6% stepped by 2%, were characterized and quantified. Finally, the effects of Ni on the microstructure and property of low-carbon bainite high-strength weld metal are summarized.

2. Experimental Procedure

The base metal employed in this study was 28 mm thickness Q345 high-strength low-alloy (HSLA) steel plate [0.2C, 1.6Mn, 0.55Si, 0.025S, 0.025P, 0.03Nb, 0.15 V and 0.1Ti (wt.%)] with the dimensions of 450 mm × 250 mm × 28 mm, which was obtained by electrical discharge cutting machine (EDCM) process. The mechanical properties are represented in Table 1.

Table 1 Properties of Q345

σ_b/MPa	σ_y/MPa	A_{kv}/J	δ/%
470–650	259–324	≥ 34	≥ 22

σ_b is the tensile strength, σ_y is the yield strength, A_{kv} is the Charpy V toughness, δ is the elongation

Table 2 Compositions of weld-deposited metal (wt.%)

Sample	C	Mn	Si	S	P	Cr	Ni	Mo	V	Cu
Ni0	0.045	1.62	0.3	0.007	0.01	0.69	0.01	0.87	0.0028	0.012
Ni2	0.063	1.5	0.26	0.0089	0.014	0.68	1.96	0.89	0.0038	0.016
Ni4	0.052	1.37	0.19	0.0095	0.013	0.61	3.65	0.92	0.004	0.017
Ni6	0.029	1.74	0.36	0.0063	0.0097	0.70	6.38	0.78	0.001	0.0031

Table 3 Parameters of welding

Shielded gas	Heat input E, KJ mm^{-1}	Deposition rate v, kg h^{-1}	Interpass temperature T,°C
95%Ar + 5% CO_2	2.0	22–68	100

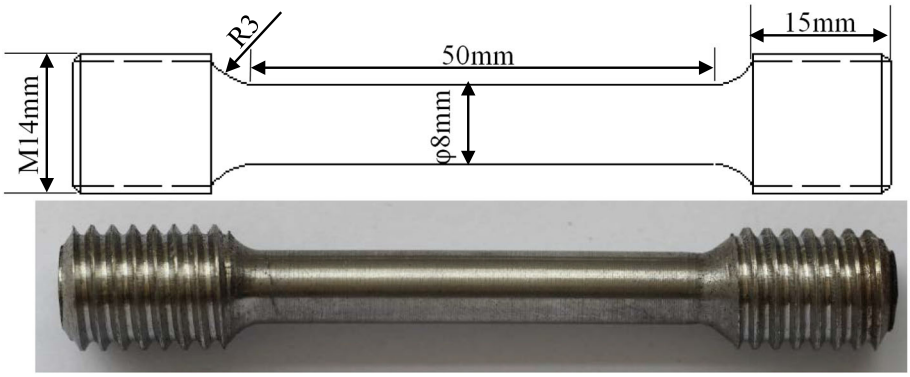

Fig. 2 Dimensions of round tensile specimens I: final pass as-deposited weld II: reheated weld metal in HAZ

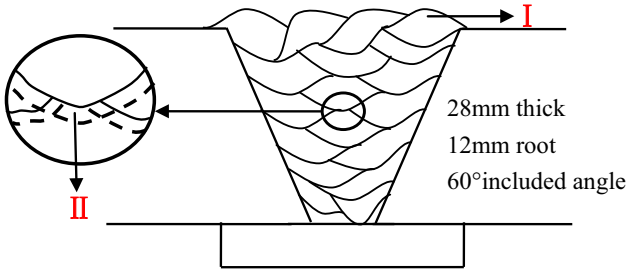

Fig. 3 Schematic of welding pass sequence

Before welding, base metal plates were cleaned using acetone in order to remove any source of contaminations like rust, dust, oil, etc.

Four metal power flux-cored wires with the diameter of 1.6 mm (Wire grade is CHT120CK4, and its type is GB/T17493E83C-K4) with Ni contents ranged 0, 2, 4, and 6% were employed as filler metals. Four weld metals with designed Ni contents were produced, the chemical compositions of which are shown in Table 2.

To avoid the dilution of the weld metal by the base metal, buttering welding was performed in 20-mm deep V-groove in the Q345 steel plate before the deposition of the first-pass weld bead. The welding regime is listed in Table 3. The multi-pass bead was deposited using a gas metal arc welding process with

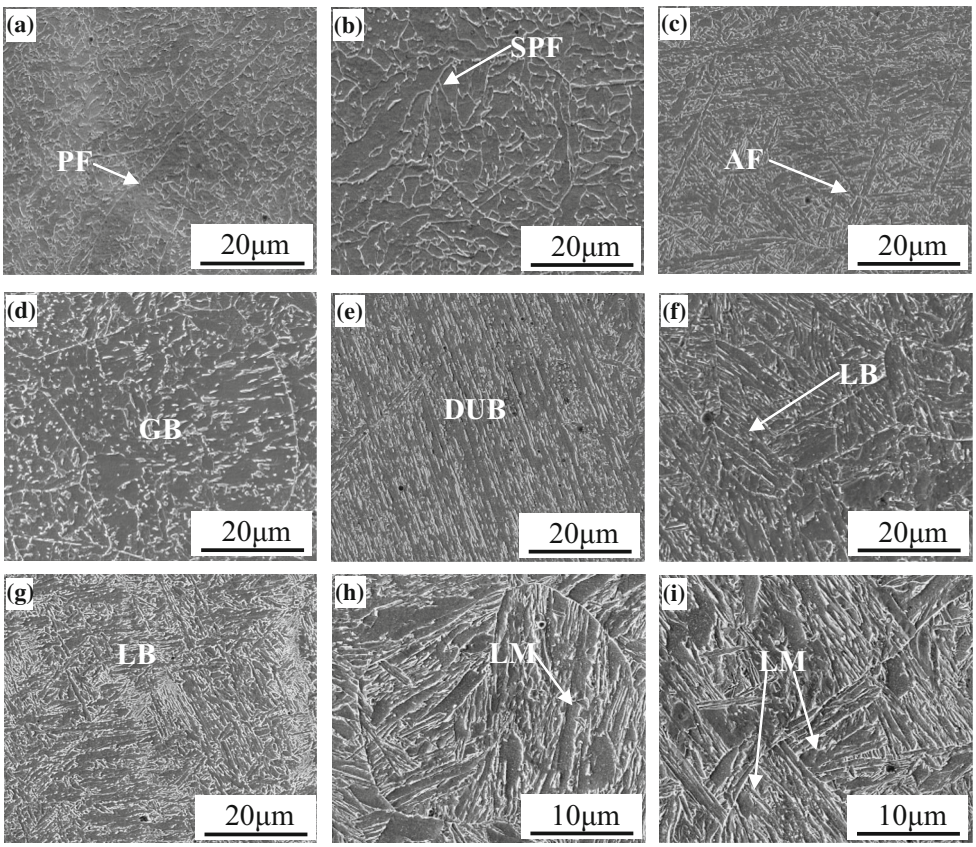

Fig. 4 Morphologies of various microstructures obtained by SEM (a) PF, (b) SPF, (c) AF, (d) GB, (e) DUB, (f) LB, (g) LB, (h) LM and (i) LM

a heat input of approximately 2.0 kJ·mm^{-1}. The interpass temperature of 100 °C and the shielded gas of 95%Ar + 5%CO_2 were selected.

After welding, metallographic specimens were cut from the weld joints using an electrical discharge cutting machine. Then, the specimens were grinded, polished, then etched using a solution of 3% nitric acid in ethanol for observation. The columnar crystals and detailed microstructural observations were carried out using OM (OLYMPUS BX51-P), SEM (FEI quanta 450), TEM (JEM-200CX), respectively. Tensile tests were carried out by the tester SHIMADZUAG-10T at room temperature (RT) −50, −80, −110, and −196 °C. Special round specimens with a gage size of 8 mm in diameter and 50 mm in length, which just covered the size of weld metal, are designed as shown in Fig. 2. Micro-hardness was measured by micro-hardness tester (HVT-1000A) (0.05 kg). The relief produced by laser confocal microscope was used to identify the black plane appearing between lath packets.

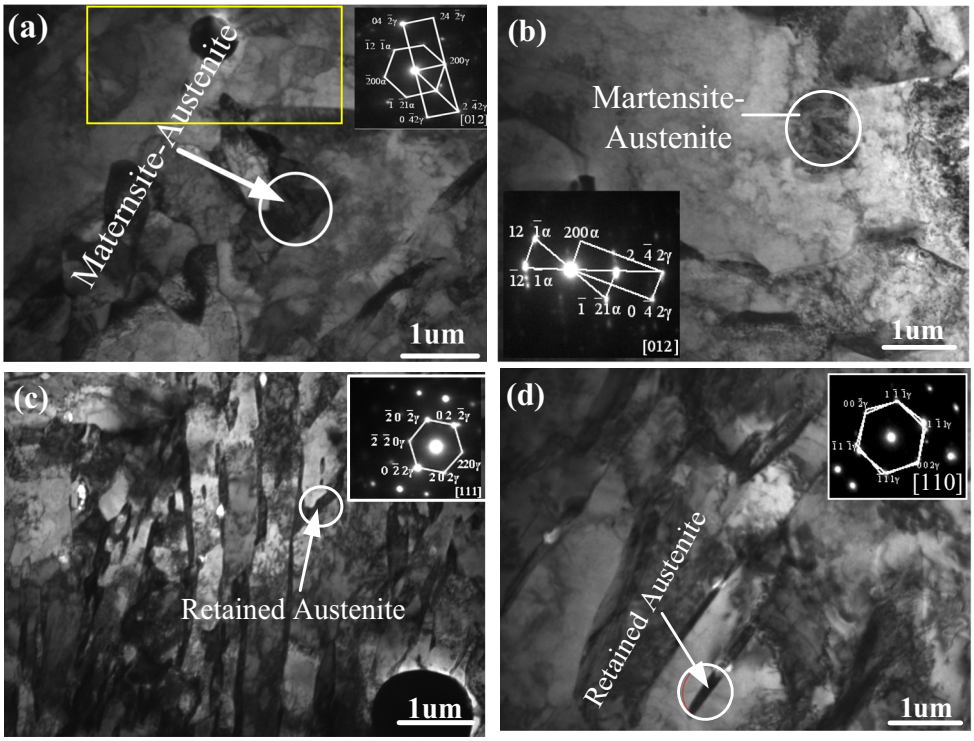

Fig. 5 Morphologies of various microstructures obtained by TEM—(a) AF and M-A, (b) M-A, (c) LB and RA, (d) LM and RA; The inclusion in (a) provides a nucleation site for AF, and the surrounding ferrite grows as a snow shape indicated by yellow rectangle (Color figure online)

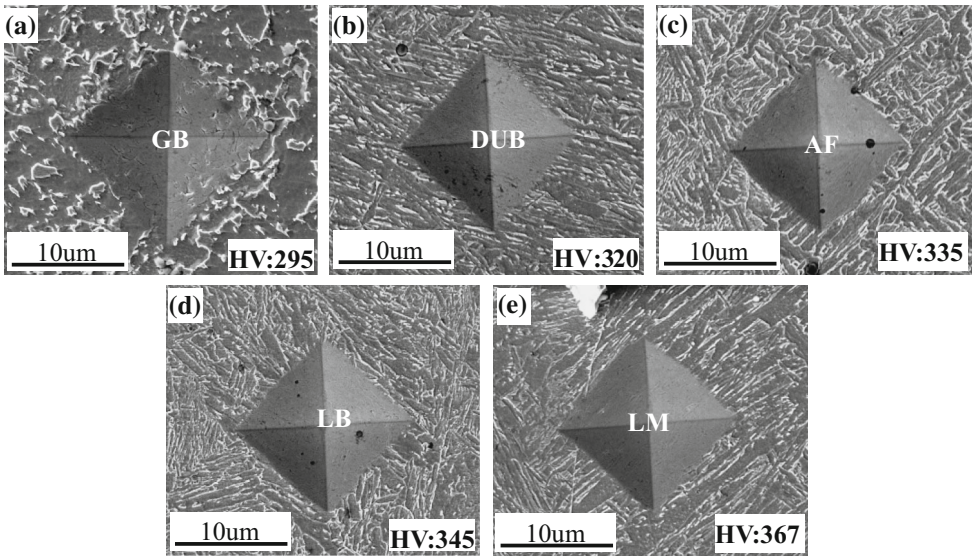

Fig. 6 Indents of micro-hardness on various microstructures by SEM (a) GB, (b) DUB, (c) AF, (d) LB and (e) LM

As the deposited weld metal specimens were obtained by multi-pass welding, the microstructure in each pass differs greatly. The latter passes reheated the former passes to some extent, which made difference between the reheated and the as-deposited weld (Ref 17). In this work the microstructure were divided into two typical areas, i.e., the final pass as-deposited weld (Zone I in Fig. 3) and reheated weld metal (Zone II in Fig. 3) in HAZ in the multi-pass weld-deposited metal shown in Fig. 3, respectively.

3. Results and Discussion

3.1 Classification Scheme Used to Identify Characteristics of Microstructures in Multi-pass-Welded Metal

3.1.1 Microstructural Characterization by Morphology. Microstructures were identified according to the classification scheme illustrated in Fig. 4 and 5, which were developed from a review of SEM and TEM studies performed on weld-deposited metal (Ref 18). In Fig. 4 and 5, representative micrographs illustrating the main features of the main microstructural constituents found in low-carbon steel weld metal are presented. As shown in Fig. 4 (a), PF precipitates in the austenite boundary, along the direction of its stretching. In contrast, as SPF nucleates in the austenite boundary, there occurs internal growth of side plates shown in Fig. 4(b). In Fig. 4(c), AF presents snowflake, and its nucleation site where stands an inclusion always lies in the grain interior. Besides, its snowflake-like ferrite plats radiating from an inclusion are observed in TEM micrograph of Fig. 5(a). In Fig. 4(d), GB consists of large quantities of M-A) constituents in the shape of bulk and short strip scattering on the base of ferrite. Its TEM micrograph can as well be seen in Fig. 5(b). The dark particles of M-A with higher density are distinctly exhibited in accordance with Li et al. (Ref 19). When M-A constituents lying on the ferrite are distributed in parallel, they turn to interval linearly arranged intermittent short strips as shown in Fig. 4(e), it will be called DUB (degenerate upper bainite), which is different from the traditional bainite. DUB reduces the

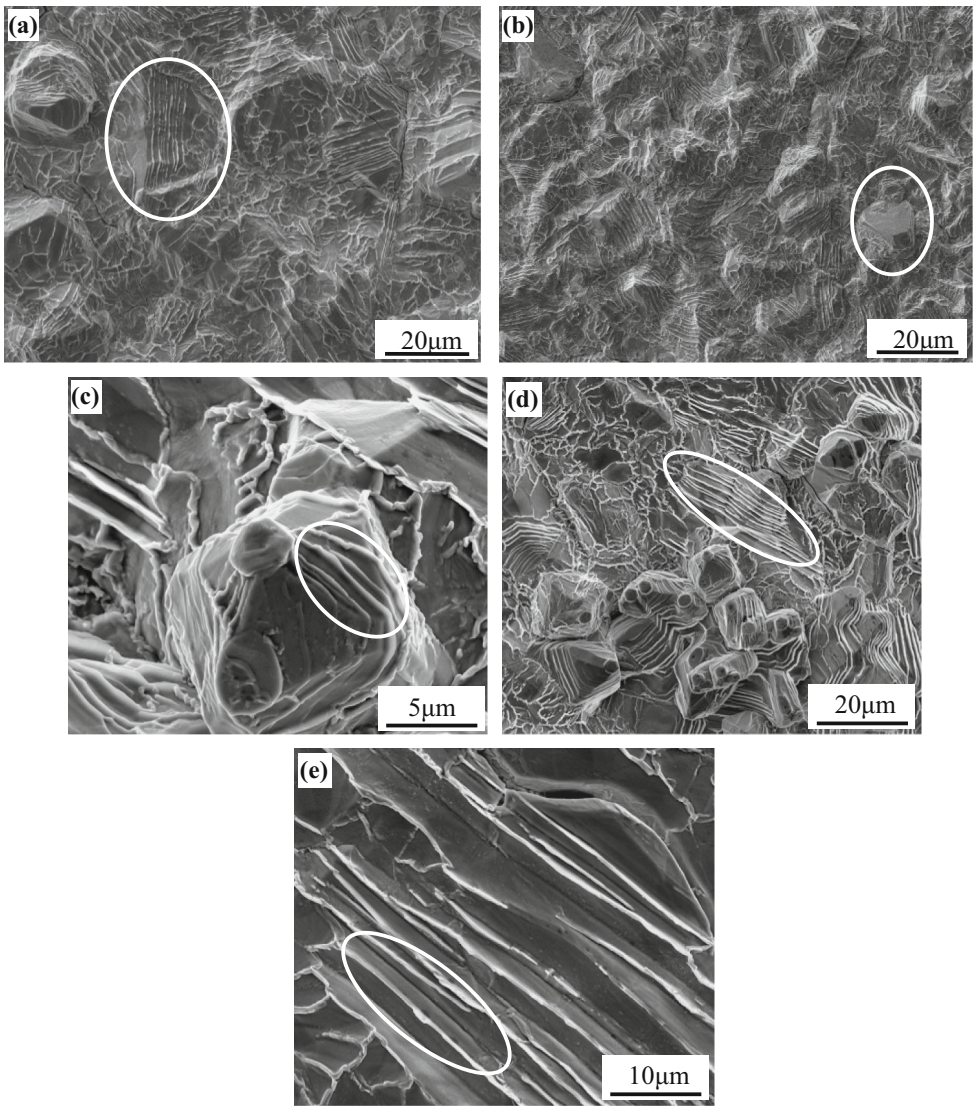

Fig. 7 Surface topography produced by laser confocal experiment (LSCM)—white circles in (a), (c) and (d) illustrate bainite laths perpendicular to observation surface, white circle in (b) indicates broad surface of lath bainite parallel to observation surface, and white circle in (e) displays tent-shaped surface relieves

existence of microcrack on condition that carbide has not constantly precipitated along austenite grain boundaries or between bainite laths, which makes its strength match toughness best (Ref 20). As for LB shown in Fig. 4(f) and (g), it is made up of lath bainite ferrite ranging side by side, and RA distributing between the laths with the shape of thin slice, which is very beneficial to improve the toughness of the material. Meanwhile, Fig. 4(h) and (i) shows distinct morphologies of LM. In addition, both LB and LM, whose TEM micrographs are shown in Fig. 5(c) and (d), respectively. Both LM and LB nucleate on the boundary of grain where they grow toward in, besides, they also nucleate from the laths that have already formed. By comparing Fig. 5(c) and (d), it is found that the lath width of LM seems wider than that of LB and the density of dislocation is higher. Besides the difference of lath width between the LB and LM, the difference in SEM image deems to be that the laths of martensite show continue straight strips across the domain decorated by grain boundaries or the boundaries defined by preceding LM as seen in Fig. 4(h) and (i). The laths of LB show some intermittent sheaves, which are not so straight as those of LM. And the growth of LB could be stopped inside a grain. However, in general, the differences between the lath morphologies between LB and LM are not so distinct that to distinguish LB from LM definitely. The hardness test is a strong tool to be a supplement.

3.1.2 Identifying the Microstructure by Hardness. Because some microstructures are similar in the view of morphologies, especially the lath bainite and lath martensite, some cases DUB as well, the change interval of micro-hardness value related with microstructure can be used as a strong tool to

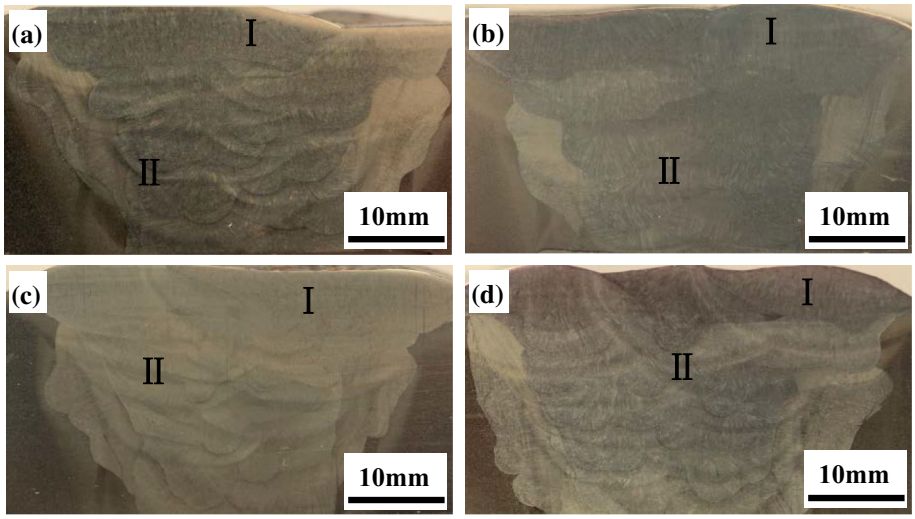

Fig. 8 Features of macroweld metal obtained by OM (a) Ni0, (b) Ni2, (c) Ni4 and (d) Ni6 (b) I: final pass as-deposited weld II: reheated weld metal in HAZ

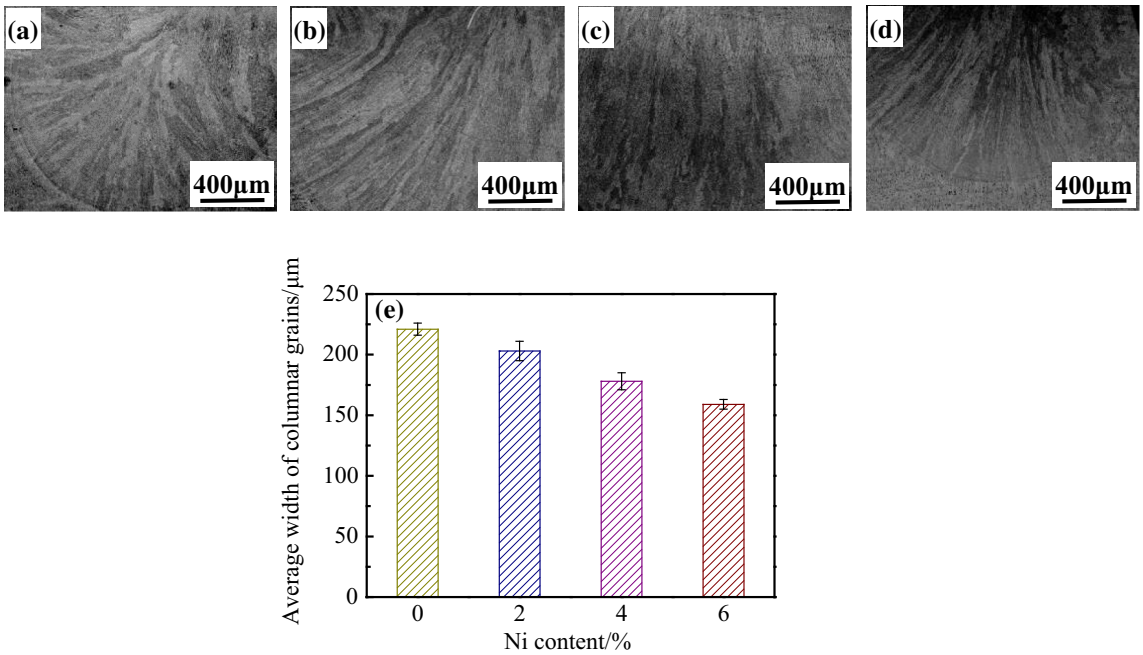

Fig. 9 Morphology of columnar grains in the weld metal samples by OM of (a) Ni0, (b) Ni2, (c) Ni4, (d) Ni6 and (e) average width of columnar grain

identify the microstructural character. As shown in Fig. 6(a), (b), (c), (d) and (e), the phases of GB, DUB, AF, LB, and LM show various hardness values HV of 295 (standard deviation: 10), 320(12), 335(9), 345(11), and 376 (11), respectively, the data of which were calculated with 45 indents per phase-field. These hardness values are very useful to distinguish the LB from the LM even though the data are not very accurate.

3.1.3 Relief Produced by Laser Confocal Microscope is Used as a Supplemental Tool. The black plane appearing between lath bainite and lath martensite, as shown in Fig. 1 and 4(f), (g), (h) and (i), has been referred as coalesced bainite, evolved by the coalescence of finer bainite platelets, each of which is separately nucleated but in the same crystallographic orientation during prolonged growth (Ref 21). This could therefore be regarded as lower bainite (Ref 10). In (Ref 11), these black facets were claimed as tempered martensite. By using the laser confocal microscope, the specimens that was polished without etching were heated to peak temperature of 1350 °C and then cooled at a cooling rate of 8 °C/s, and the relieves were produced and exhibited in Fig. 7. In Fig. 7(a) a relief produced by a lath martensite packet is noted by a white circle. It is revealed that the martensite laths growing perpendicularly or declining with a large angle with the polished surface show a bundle of parallel white strips, while the side

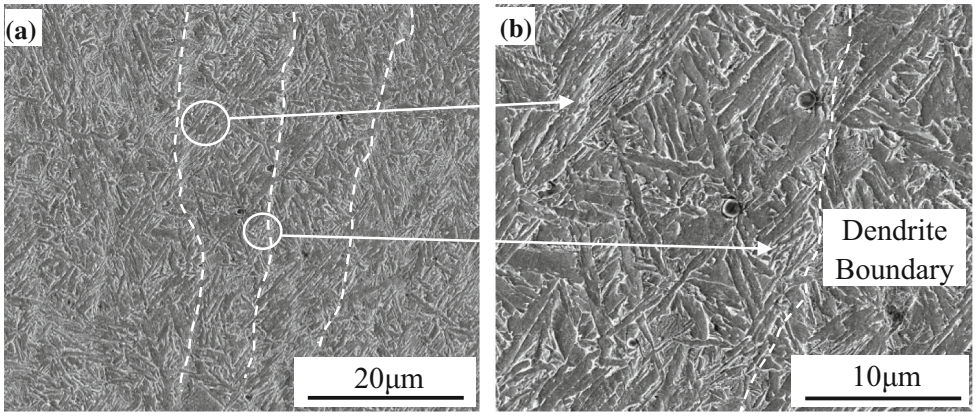

Fig. 10 Morphology of columnar structure obtained by SEM

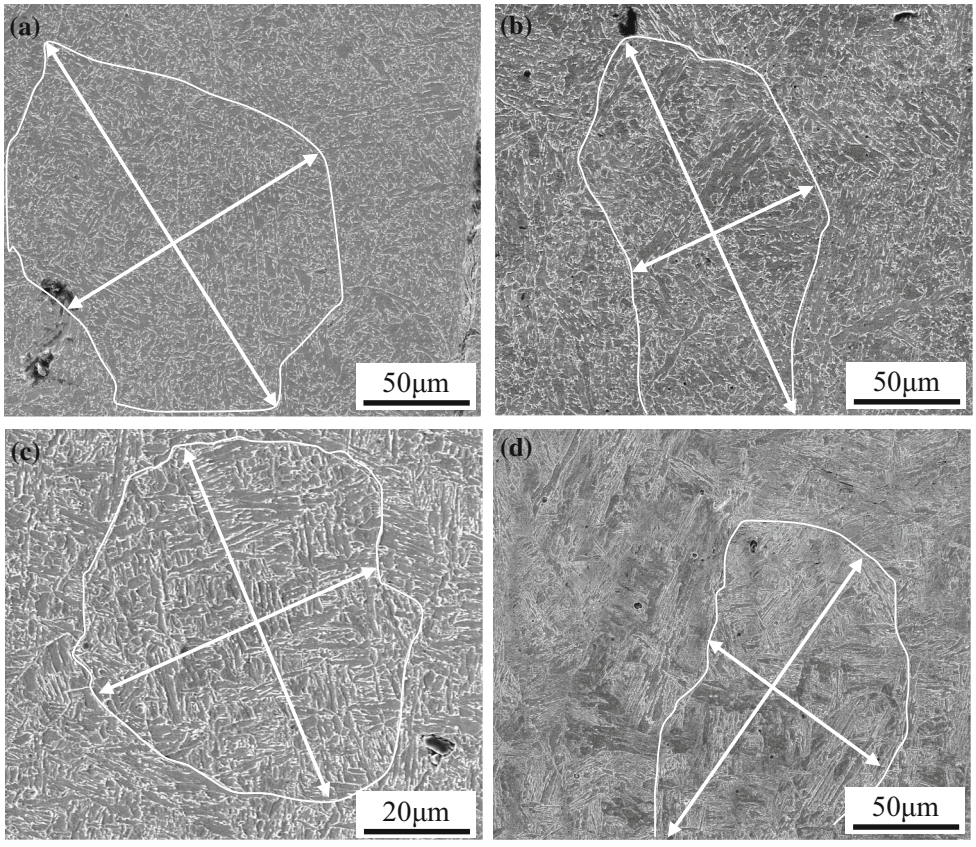

Fig. 11 Prior austenite grains in the specimens with Ni mass fraction of (a) 0%, (b) 2%, (c) 4%, and (d) 6% depicted by picric acid etching—white lines represent prior austenite grain boundary; macroaxis and brachyaxis arrows are drawn for calculating average grain size

face of the martensite lath exhibits a black plate. Figure 7(b) and (c) displays two relieves of martensite packets (noted by white circles). It is apparent that the sheaves (laths) in the packets grow in the direction parallel or declined with a small angle with the polished surface. The observed black plates are the side surface of one sheaf (lath). In Fig. 7(d), a lot of relieves display the martensite packets growing in parallel directions (noted by a white circle). From these observations, it is convinced that if the polished surfaces were etched, the side surfaces of the laths of martensite shown in Fig. 7(a), (b), (c) and (d) should appear as black plane facets. That is, the black facets observed in Fig. 1 and 4(f), (g), (h) and (i) are the side surfaces of sheaves (laths) which grows parallel or with a small angle inclined with the specimen's surface. When the martensite laths grow perpendicular or with a large angle inclined to the specimen's surface, after etching they will present as the feature of lath packet, while when the martensite laths grow parallel or with a small angle inclined, they will present as black plane facets after etching. Then in conclusion the black plane facets appearing between martensite lath packets are the side surfaces of the martensite lath. In addition the values of micro-hardness higher than HV360 further prove that the black plane facets shown in Fig. 6(e) should be martensite. Moreover, tent-shaped surface relieves of lath martensite shown in Fig. 7(e) by a white circle, the mechanism of martensite phase transformation can be explained as the transition of lattice reorganization due to a collaborative, directional, and orderly displacement of the whole atoms' group (Ref 22).

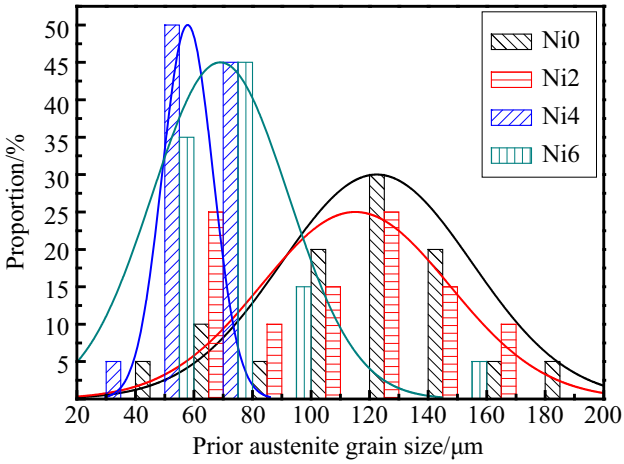

Fig. 12 Distributions of prior austenite grains in the specimens with Ni mass fraction of (a) 0%, (b) 2%, (c) 4%, and (d) 6%, respectively

3.2 Characterization of Weld Metal

Macroscopic weld metal features are shown in Fig. 8. In Fig. 8, as mentioned above, the weld metal was composed of two parts, one is as-deposited weld metal (top-pass weld metal) which was directly solidified from liquid metal and had not been heat-affected by other passes. The other is multi-pass weld metal which had been heat-affected by the next pass welding processes. As-deposited weld metal has significant effect on the mechanical properties of the welded joint, especially, coarse columnar grains in the as-deposited weld metal will reduce strength and toughness obviously (Ref 23). As seen in Fig. 8, there are a few differences of macrostructures of the multi-pass

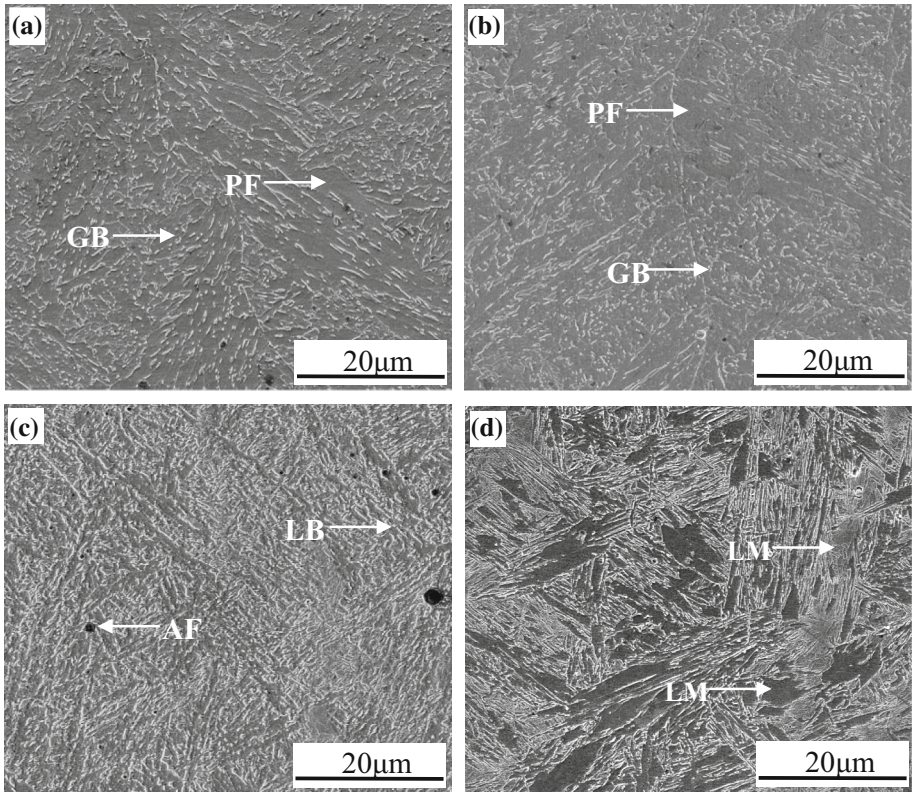

Fig. 13 Microstructure of as-deposited weld metal in the final pass of weld by SEM (a) Ni0, (b) Ni2, (c) Ni4 and (d) Ni6

weld metals with four different contents of Ni, for instance, the distinctly various weld passes and layers.

3.2.1 Columnar Grains of Weld Metal. In order to reveal the effects of Ni content on the morphology of columnar grains, the morphology of columnar grains in the weld metal with different Ni contents and their average width are observed and presented in Fig. 9. In addition, with the software Image-Pro Plus used, the data were acquired by counting the average width of five optical microscope (OM) pictures in the last weld of various Ni content specimens. Because the growth direction of columnar grain keeps identical with that of maximum temperature gradient in the solidification, the columnar grains exhibit a curved pattern following the change of the temperature gradient. In Fig. 9(e), the average width of columnar grains reaches more than 200 μm in Ni0 specimen, yet it shows a decreasing trend with the increase in Ni content.

When the weight content of Ni increases to 6%, its macrostructures show a columnar structure, as shown in Fig. 10(a), a great number of martensite packets with acicular ferrite strips distribute inside of the column grain (Fig. 10b). The interfaces of strips and martensite packets are not straight lines but curves in different diameters, and there exist wide mutual variations between thickness and length of each strip, which can be seen in Fig. 10(b). On the boundaries of columns (pointed by dashed lines in Fig. 10a), dense parallel martensite laths are observed (pointed by white arrows in Fig. 10b).Within the micrographs the weld metal dendrites that formed during weld metal solidification are clearly seen.

3.2.2 Prior Grains of Weld Metal. Li et al. (Ref 24) indicated that prior austenite grain size had important effects on final microstructure and properties. For depicting the prior austenite grains, the specimens were etched by 3% nital. The specific prior austenite grains marked by white lines in specimens with Ni fraction of 0, 2, 4, and 6% (wt.) are shown in Fig. 11. The sizes of the prior austenite grains are measured as the average value of the two lengths measured by the two arrows perpendicular to each other in Fig. 11. Nearly 40 micrographs with 400 grains were chosen to measure the prior austenite grain size of each specimen, and Fig. 12 represents the corresponding proportion distributions of prior austenite grain sizes in weld metal, and the coarsest austenite grain sizes in specimens with Ni fraction of 0, 2, 4, and 6% (wt.) are 186, 170, 72, and 136 μm, respectively.

3.2.3 Microstructural Characterization of Weld Metal. In this section on the base of section 3.1, detailed microstructural analyses are carried out on the cross sections of metallographic specimens.

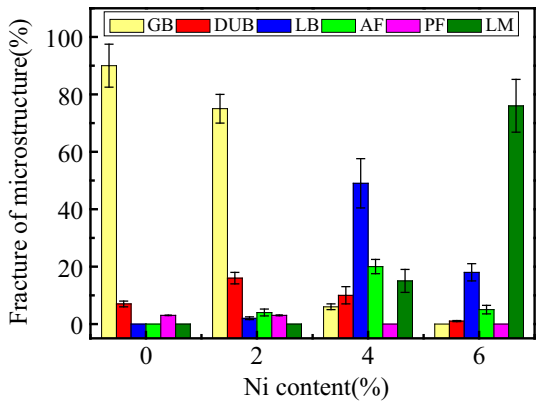

Fig. 15 Fraction of microstructure in the weld-deposited metal (%)

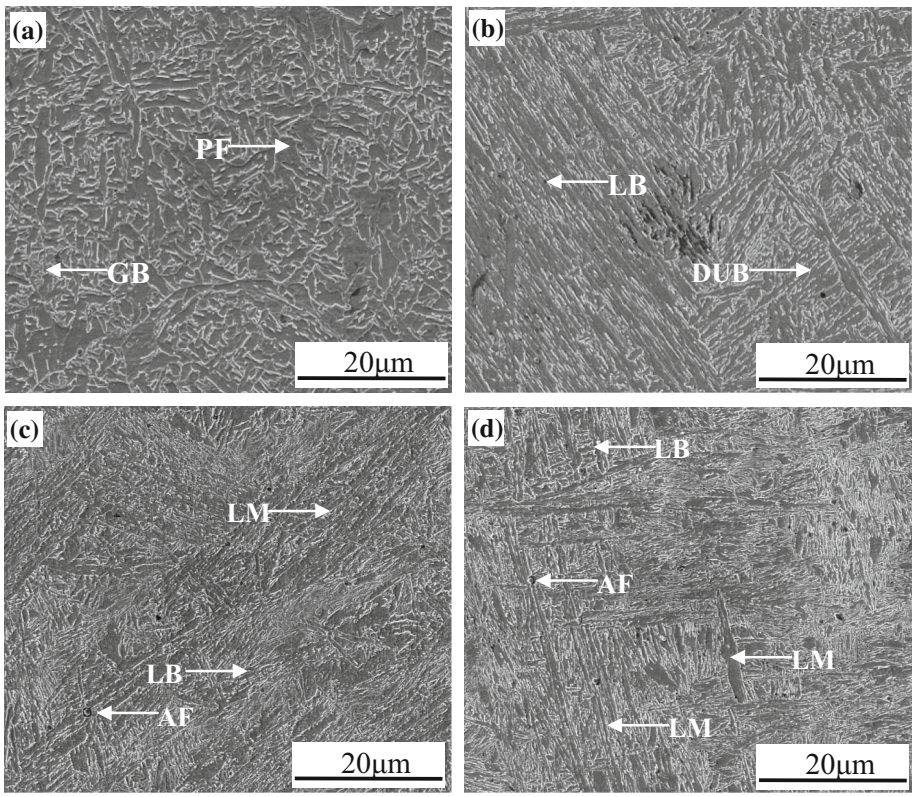

Fig. 14 Microstructure of internal HAZ in the weld-deposited metal by SEM (a) Ni0, (b) Ni2, (c) Ni4 and (d) Ni6

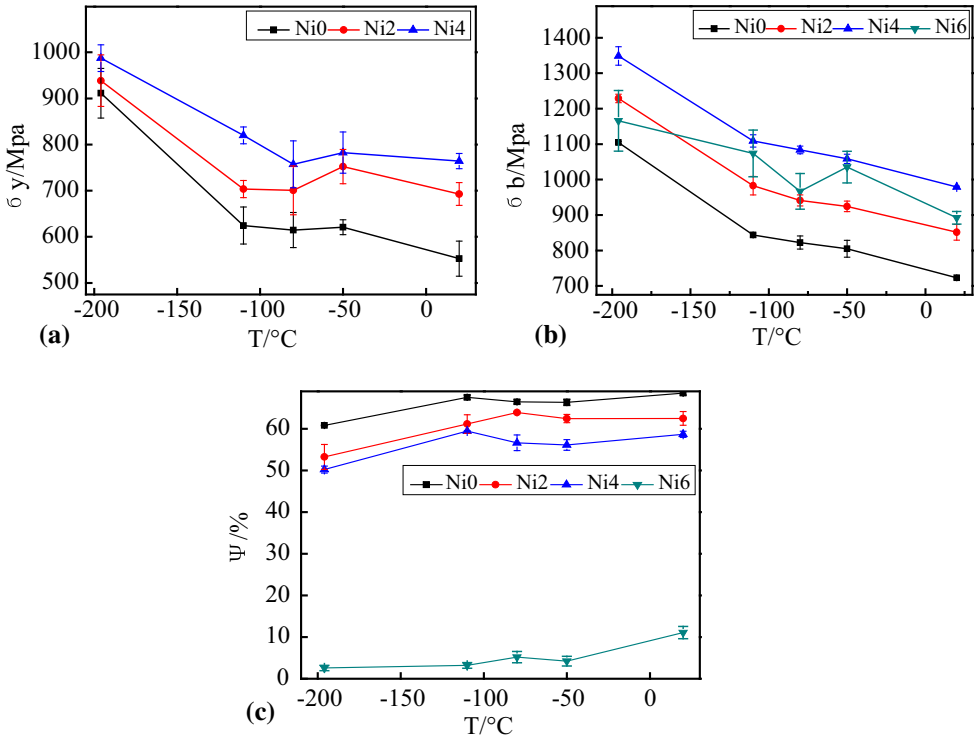

Fig. 16 Variations of (a) yield strength (b) ultimate tensile strength (c) reduction of fracture region with temperature in weld metal specimens with Ni mass fraction of 0, 2, 4, and 6%, respectively

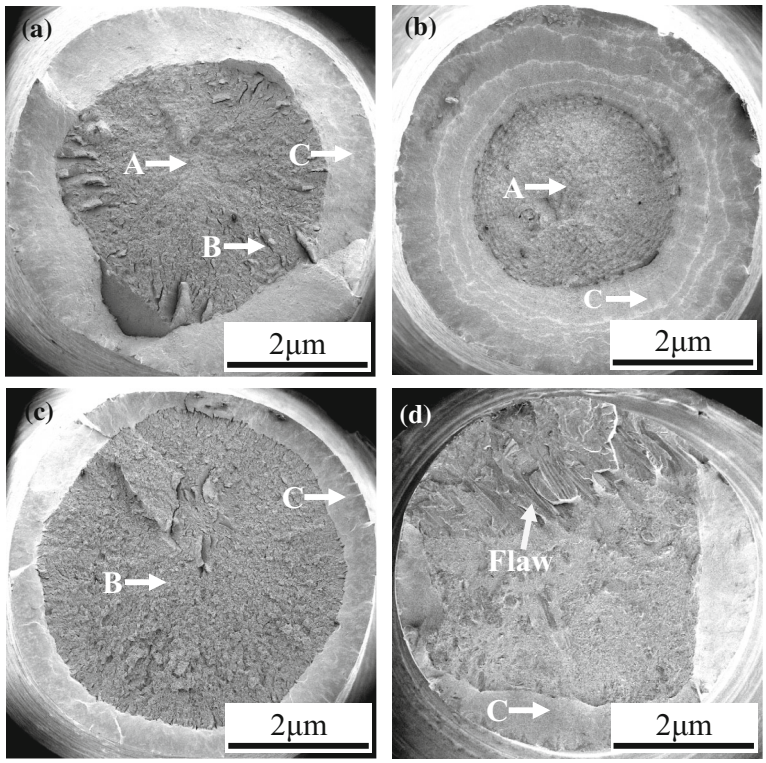

Fig. 17 Four representative fracture surface morphologies of various specimens—A: fiber region, B: extension region, and C: shear lip, respectively; (a) standard specimen fracture with three regions, (b) specimen fracture with fiber region and shear lip, (c) specimen fracture with extension region and shear lip, and (d) specimen fracture with flaw and shear lip

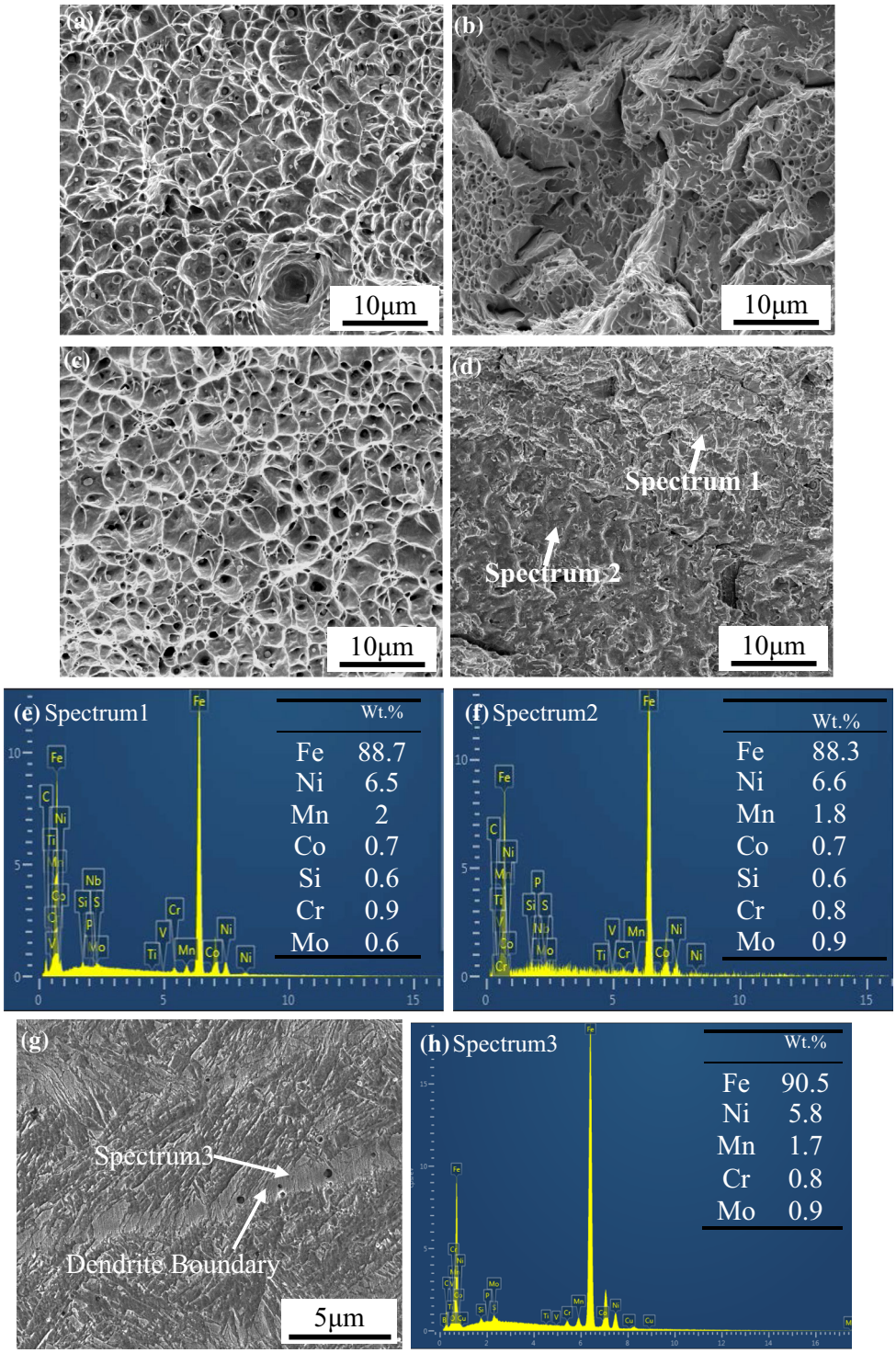

Fig. 18 Typical areas magnification of fracture surface—(a) fiber region, (b) extension region, (c) shear lip, (d) flaw region, (e, f) EDS results taken from (d), (g) microstructure of flaw area and (h) EDS results taken from (g), respectively

With the cooling process, solid phase transformation proceeds. Figure 13 displays the microstructures of the as-deposited weld metal with various Ni contents. The microstructures of the heat-affected zone reheated by next passes are shown in Fig. 14.

From Fig. 13 and 14, the following results are summarized: In the sample of Ni0, the microstructures of weld metals in both as-deposited and reheated zones consists of majority of GB, where numerous M-A particles distributed on the base of ferrite. Certain PF exists. When the content of Ni increases to 2%, GB is still dominant, some DUB and LB generates in the reheated zone of inner weld. And due to the low carbon content, the carbide precipitation is restrained during bainite transformation. In consequence, a typical ULCB with the retained austenite slices (instead of the carbide) distributed between bainite laths generates in Fig. 5(c). The microstructure

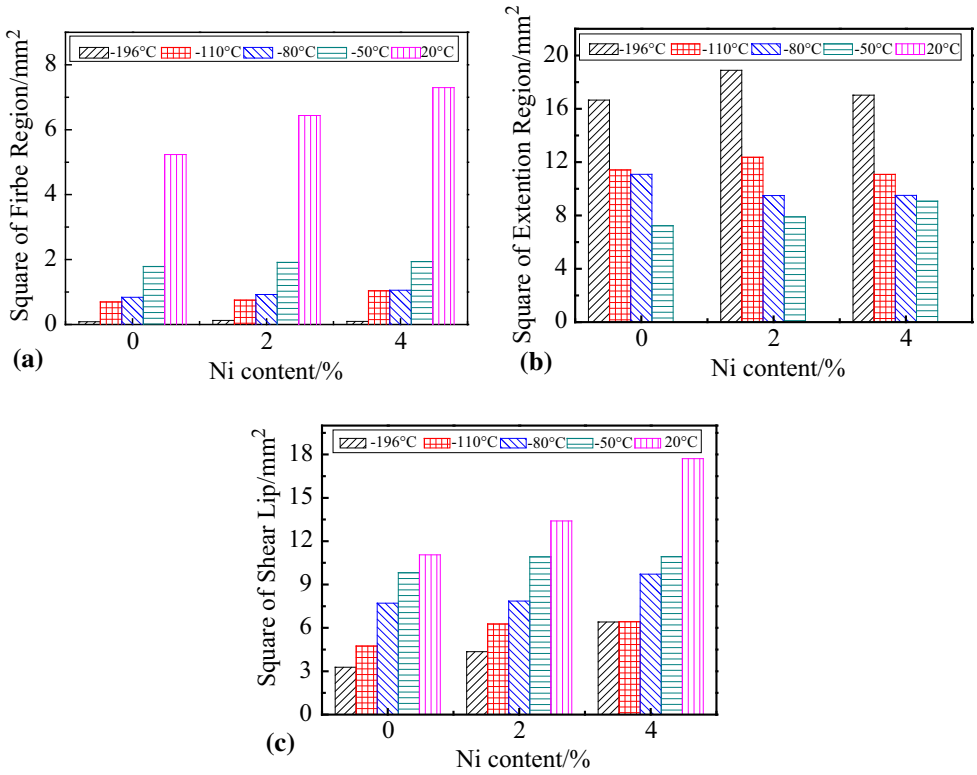

Fig. 19 Square variation of three areas with the increment of Ni content and test temperatures—(a) fiber region, (b) extension region, and (c) shear lip, respectively

of sample Ni4 after continuous cooling transformation consists of dense LB and LM with minor AF shown in Fig. 13(c) and 14(c), and considerable tiny inclusions are distributed in the deposited weld metal, some of which exist in inner laths and others can be found inter laths. AF extends to grow from this kind of inclusions.

The Ni6 specimen mainly contains LM with some LB and minority of AF. Two kinds of morphologies of LM can be observed: One appears as a morphology of black plane facets (pointed by the white arrow in Fig. 13d and Fig. 14d). As analyzed in section 3.1 and in Tan and Ma (Ref 25), the black plane (facets) appears once the polished surface is parallel or declined with a small angle with the side surface of the martensite lath. The other morphology appearing in Fig. 14(d) appears in parallel interval white laths when the polished area of specimen becomes nearly perpendicular to the martensite laths. When the habit plane is vertical with the polished facet, monochrome bundles of lath martensite microstructure appear with the same color, which are mainly caused by three aspects: (i) the basically same atoms distribution on both sides of twins surface, and (ii) the identical amount and width of the cross-sectional interface of lath grains causing the similar degree of corrosion in each block side (Ref 26).

Based on the microstructural characterization, the fractions of different microstructures phases in the weld metal with different content of Ni in the wire were measured by means of the software Image-Pro Plus, and more specifically, five SEM pictures of each content of Ni were chosen to count via quantitative metallography, as shown in Fig. 15, which showed that GB content decreases, LM content increases with the increasing of the Ni content.

3.3 Tensile Property Analysis

Figure 16 plots the variation of the yield strength (YS), UTS, and reduction of fracture area against the temperature for weld metal specimens. Each data was obtained according to three samples. For instance, as the Ni content was 4%, when it came to −196 °C, there were three identical specimens used for that experiment. From Fig. 16(a) and (b), the yield strength and UTS decrease with the decreasing Ni mass fraction and the increasing test temperature. It is notably interesting to find that variation curve of Ni6 sample disappeared in Fig. 16(a). Combined Fig. 17(d) with Fig. 18(d), (e) and (f), the flaw area presenting "scrape style" on the fracture surface was analyzed by EDS, the result of which revealed alloy elements (i.e., Ni, Mn, and Cr et al.) segregation occurred there. Meanwhile, microstructure characteristic of flaw area depicts the weld metal dendrites boundary (Fig. 18g) where identical elements segregation phenomenon also emerged (Fig. 18h), and the mentioned results keep in accordance with what Fig. 10 depicts. From another perspective, brittle fracture took place and the strength could not reach yield limit due to the existence of flaw in Ni6 specimen. The lath-like or plate-like acicular ferrite grains can divide large austenite grain into smaller separate regions (Ref 27). The bainite transformed at lower temperatures is thus confined in the smaller regions, resulting in the formation of fine-grained mixed microstructures (Ref 28). The mean and standard deviation equivalent diameters of grains in Ni4 specimen were smaller than those in any other specimen (Fig. 11), which means that the grain in Ni4 specimen was smallest. Fine-grain strengthening can be calculated under empirical equation (Ref 29), which is given by,

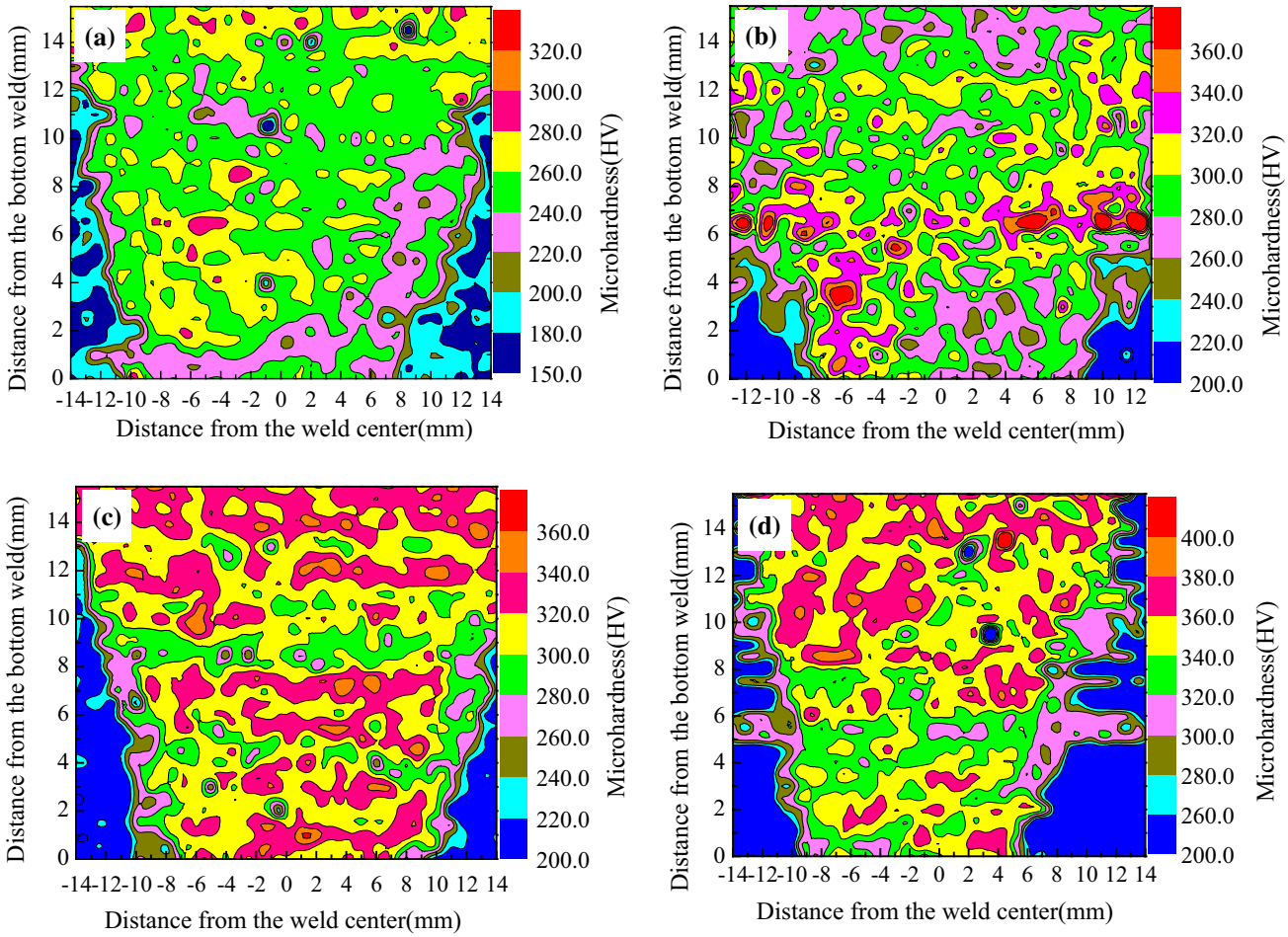

Fig. 20 Distribution of micro-hardness on the surface of metallographic samples (a) Ni0, (b) Ni2, (c) Ni4 and (d) Ni6

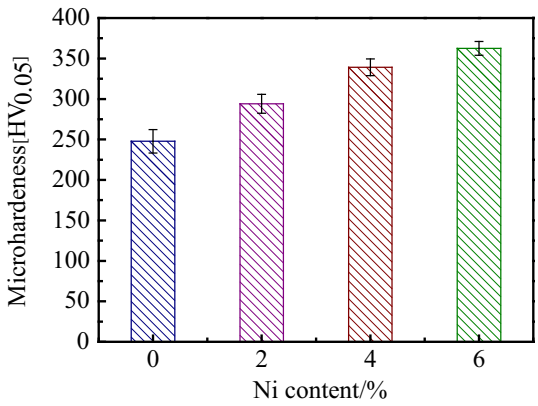

Fig. 21 Variation of average micro-hardness of deposited metal

$$\sigma = k \cdot d_g^{-1/2} \quad \text{(Eq 1)}$$

where σ is the strength improved by grain refinement, d_g is the effective diameter of grain, and k is parameter [usually seen as 17.4 N mm$^{-3/2}$ in high-strength low-alloy steels (Ref 30)]. The difference of strength by grain refinement among four specimens is in agreement with the result of measured strength shown in Fig. 16(a) and (b). The reduction of fracture region increases with the decreasing Ni content and the increasing test temperature in Fig. 16(c).

Four representative fracture surface morphologies of various specimens at different test temperatures are shown in Fig. 17. Region A, B, and C were respectively defined as fiber region, extension region, and shear lip, while Fig. 17(d) depicts real flaw region in Ni6 specimen. Therefore, it is unnecessary to study the tensile property of Ni6 specimen by means of three regions mentioned above. Magnification of three regions is shown in Fig. 18(a), (b) and (c), respectively. The fracture mode of fiber region and shear lip is ductile rupture with dimple pattern for all specimens at any test temperature. The width and depth of the dimples seem to decrease in shear lip compared with that of fiber region; however, no significant variation can be distinguished. Extension region shows obvious radiation (shear) pattern, a typical shear ridge and a signal of shear tearing with low energy (Ref 31). As shown in Fig. 19(a) and (c), Squares of fiber region and shear lip increase, respectively, with the increasing Ni content and test temperature, which extends constriction time. Meanwhile, the reduction of fracture area was enlarged except Ni6 specimen (corresponding value lower than any other specimen) in Fig. 16(c). On the contrary, the square of extension region decreases (Fig. 19c), especially extension region even disappeared at RT (20 °C).

3.4 Micro-hardness Analysis

Further identification of microstructure in multipass weld metal was also carried out by micro-hardness tests. To make sense of the relationship between micro-hardness and microstructure, the hardness tests have been made on the metallographic section surface of nearly 1824 points for each specimen on which 0.49 kN was loaded lasting for 15 s. On each surface, 32 lines with 57 points separated at the distance of 0.5 mm for each line were set. Finally, four cloud images indicating the distribution of micro-hardness are made for each specimen as shown in Fig. 20.

As can be clearly observed in Fig. 20, the micro-hardness presents the trend of being enlarged with the increasing content of Ni ranged from 0 to 6% by a step of 2%. Besides, average hardness values of the upper weld in the Fig. 20 indicate that the hardness of upper weld is higher than that of the lower weld.

The most important is that by comparison with Fig. 20 and the hardness values revealed in Fig. 6, the microstructures evolved in specimens are further identified: such as AF plus GB in Ni0, GB plus LB in Ni2, LB plus minor LM in Ni4, and major LM in Ni6.

As shown in Fig. 21, the average micro-hardness value reaches HV247.7 when there is bare content of Ni, whose microstructure consists of GB plus PF and AF. As the fraction of Ni increases to 2%, it adds up by HV46.4 for the formation of small amount of DUB and limited LB. Further still, it will arrive at the value of HV (0.05 kg) 339.2 with the amount of 4% Ni as a result of majority of LB transferred from DUB and generation of LM. With the microstructure transformed with large amount of LM, the hardness finally increases to HV362.5.

All the mentioned results verify the reasonability of Fig. 15 which is estimated from the phase measurements. Inversely, it is possible by incorporating the hardness values measured in Fig. 6 to estimate the distribution of the microstructure from the measured hardness cloud images.

4. Summary

After detailed observations and identifications of various microstructural phases produced in multi-pass weld metal with increasing the content of Ni by metal powder-flux-cored wire, the following results are summarized:

1. Microstructural phases have been characterized. LB is distinguished from LM by following items: chemical composition estimation, morphology difference observed by SEM and morphology difference observed by TEM, especially by different values of hardness measured by micro-hardness tests. The black plates (facets) appearing between LM (LB) packets are identified as the side faces of LM (LB) laths by LSCM and hardness value of above HV360. The black plates appear when martensite laths grow parallel or declined with a small angle with the polished surface. When the LM laths grow perpendicularly or with a large angle with the polished surface the morphology of typical bundle lath packet will be presented.
2. YS and UTS decrease while the reduction of fracture area increases with the decreasing Ni mass fraction. Abnormal conclusions drawn in Ni6 specimen can be attributed to elements segregation caused by weld defect. The effects of increasing the Ni content up to 6% are revealed as: a trend of reduction of average width of columnar grains; prior austenite grain size decreasing while increasing with higher Ni content above 4%; microstructure evolution from GB plus PF and AF to GB plus DUB to LB then LM; microstructural morphology change from granular to lath mode; transformation mechanism changes from element diffusion control to mass-directional displacement control; increase of hardness.

Acknowledgments

This work was financially supported by National Nature Science Foundation of China (No. 51675255), Pre-research of National Basic Research Program of China (2014CB660810), and the Rose Willow Outstanding Individual Programs of Lanzhou University of Technology (J201203).

References

1. Seamless Steel Pipe and Method for Manufacturing the Same. A1, United States Patent Application, 2013, 0000790
2. B.G. Tang, Challenge on Weld Materials from the Development of Modern Steel and Several Advice, *Welding*, 2009, **12**, p 20–25 (in Chinese)
3. M.K. Graf and H.G. Hillenbrand, High-Strength Large-Diameter Pipe for Long-Distance High Pressure Gas Pipelines, *IJOPE*, 2004, **14**, p 117–121
4. W.W. Bose-Filho, A.L.M. Carvalho, and M. Strangwood, Effects of Alloying Elements on the Microstructure and Inclusion Formation in HSLA Multipass Welds, *Mater. Charact.*, 2007, **58**, p 29–39
5. D.P. Fairchild, M.L. Macia, N.V. Bangaru, and J.Y. Koo, Girth Welding Development for X120 Linepipe, *IJOPE*, 2004, **14**, p 1–3
6. G.M. Evans and N. Bailey, *Metallurgy of Basic Weld Metal*, Abington Publishing, Cambridge, 1997, p 178–179
7. V.T.T. Miihkinen and D.V. Edmonds, Microstructural Examination of Two Experimental High-Strength Bainitic Low-Alloy Steels Containing Silicon, *Mater. Sci. Technol.*, 1987, **3**, p 423–431
8. P.T. Oldland, C.W. Ramsay, D.K. Matlock, and D.L. Olson, Significant Features of High-Strength Weld Metal Microstructures, *Weld. J.*, 1989, **68**, p 159–168
9. A.F. Gourgues, H.M. Flower, and T.C. Lindley, Electron Backscattering Differaction Study of Acicular Ferrite, Bainite and Martensite Steel Microstructures, *Mater. Sci. Technol.*, 2000, **16**, p 28–40
10. J.H. Park, H.K.D.H. Bhadeshia, L. Karlsson, and E. Keehan, Coalesced Bainite by Isothermal Transformation of Reheated Weld Metal, *Sci. Technol. Weld. Join.*, 2008, **13**, p 593–597
11. C.Y. Wang, Y. Chang, J. Yang, K.M. Zhao, and H. Dong, The Combines Effect of Hot Deformation Plus Quenching and Partitioning Treatment on Martensite Transformation of Low Carbon Alloyed Steel, *Acta Metall. Sin.*, 2015, **51**, p 913–919 (in Chinese)
12. S.G. Park, K.H. Lee, K.D. Min, M.C. Kim, and B.S. Lee, Characterization of Phase and Misorientations on Tempered Bainitic/Martensite Ni-Cr-Mo Low Alloy RPV Steel with Various Ni Content, *Met. Mater. Int.*, 2013, **19**, p 49–54
13. Z.Y. Zhang and R.A. Farrar, Columnar Grain Development in C-Mn-Ni Low-Alloy Weld Metals and the Influence of Nickel, *J. Mater. Sci.*, 1995, **30**, p 5581–5588
14. S. Patra, S.M. Hasan, N. Narasaiah, and D. Chakrabarti, *Mater. Sci. Eng., A*, 2012, **538**, p 145–155
15. F.G. Caballero, H.K.D.H. Bhadeshia, K.J.A. Mawella, D.G. Jones, and P. Brown, Design of novel high strength bainitic steels: Part 1, *Mater. Sci. Technol.*, 2001, **17**, p 512–516

16. F.G. Caballero, M.K. Miller, C. Garcia-Mateo, C. Capdevila, and C. Garcia de Andres, Phase transformation tool for the design of advanced steels, *JOM*, 2008, **60**, p 16–21
17. Quintana MA, Babu SS, Major J, Dallam C, James M. Weld Metal Toughness-Sources of Variation, *Proceedings of the 8th International Pipeline Conference IPC*, 2010, p 1–8
18. N. Isaati, D. Jorge-Badiola, M.L. Taheri, and P. Uranga, Microstructural Features Controlling Mechanical Properties in Nb-Mo Microalloyed Steels Part I: Yield Strength, *Metall. Mater. Trans. A*, 2014, **45A**, p 4960–4971
19. X.D. Li, C.J. Shang, C.C. Han, Y.R. Fan, and J.B. Sun, Influence of Necklace-Type M-A Constituent on Impact Toughness and Fracture Mechanism in the Heat Affected Zone of X100 Pipeline Steel, *Acta Metall. Sin.*, 2016, **52**, p 1025–1035
20. V. Chaudhari, H.P. Ritzmann, G. Wwllnitz et al., German Gas Pipeline First to Use New Generation Line Pipe, *Oil Gas J.*, 1995, **1**, p 40–47
21. E. Keehan, L. Karlsson, H.K.D.H. Bhadeshia, and M. Thuvander, Three-Dimensional Analysis of Coalesced Bainite Using Focused Ion Beam Tomography, *Mater. Charact.*, 2008, **59**, p 877–882
22. H.S. Fang, J.J. Wang, Z.G. Yang, C.M. Li, X.Z. Bo, and Y.K. Zhen, *Bainitic Transformation*, Science Press, Beijing, 1999, p 100–104
23. Wang Z. Study on Microstructure and Mechanical Property in Different Metal Materials, Master thesis, 2013, p 22–25
24. X. Li, X. Ma, and S.V. Subramanian, Influence of Prior Austenite Grain Size on Martensite–Austenite Constituent and Toughness in the Heat Affected Zone of 700 MPa High Strength Linepipe Steel, *Mater. Sci. Eng.*, 2014, **616**, p 141–147
25. Y.H. Tan and Y.X. Ma, *New Morphology of Martensite*, Metallurgical Industry Press, Beijing, 2014, p 42–52
26. Y.H. Tan and Y.X. Ma, *New Morphology of Martensite*, Metallurgical Industry Press, Beijing, 2014, p 53–54
27. X.L. Wan, R. Wei, and K.M. Wu, Effect of Acicular Ferrite Formation on Grain Refinement in the Coarse-Grained Region of Heat Affected Zone, *Mater. Charact.*, 2010, **61**, p 726–731
28. X.L. Wan, K.M. Wu, G. Huang, and R. Wei, In Situ Observations of the Formation of Fine-Grained Mixed Microstructures of Acicular Ferrite and Bainite in the Simulated Coarse-Grained Heated-Affected Zone, *Steel Res.*, 2014, **2**, p 243–250
29. N. Hansen, Hall-Petch Relation and Boundary Strengthening, *Scr. Mater.*, 2004, **51**, p 801–806
30. X. Mao, X. Huo, X. Sun, and Y. Chai, Strengthening Mechanisms of a New 700 MPa Hot Rolled Ti-Microalloyed Steel Produced by Compact Strip Production, *J. Mater. Process. Technol.*, 2010, **210**, p 1660–1666
31. Y.J. Yan, R. Cao, W.S. Du, Y. Peng, Z.L. Tian, and J.H. Chen, Tensile Fracture Tests of a 980 MPa High Strength Steel at Various Temperatures, *J. Mater. Sci. Eng.*, 2009, **27**, p 246–249